JOURNAL OF SOLID STATE CHEMISTRY **126,** 271–286 (1996)
ARTICLE NO. 0338

Nanostructural Transitions Related to Flexible Shearing Phenomena in the Superconductors $Hg_{1-x}V_xSr_{4-y}Ba_yCu_2O_{7-\delta}CO_3$

M. Hervieu,[1] D. Pelloquin, S. Malo, C. Michel, and B. Raveau

Laboratoire de Cristallographie et Sciences des Matériaux, ISMRA-Université de Caen, Boulevard du maréchal Juin, 14050 Caen Cedex, France

Received May 28, 1996; accepted August 5, 1996

The HREM study of the superconducting copper oxycarbonates $Hg_{1-x}V_xSr_{4-y}Ba_yCu_2O_{7-\delta}CO_3$ ($0.28 \leq x \leq 0.40$; $0 \leq y \leq 2.65$) shows the extraordinary nanostructural flexibility of these materials. Starting from the [S_2CC] [1201] intergrowth for $y = 0$, coexistence of (100) and (110) CSP, in the form of isolated defects, is evidenced for $0 < y < 1.8$ and curved crystallographic shear boundaries are observed, for $y = 1.8$. The (110) collapsed structure is obtained for $1.8 < y < 2.5$, whereas twinned (110) CSP and mixed (110)/(110) CSP appear around $y = 2.5$, the (100) collapsed structure being synthesized for $2.50 < y \leq 2.65$. Beyond $y = 2.65$, phasoïds corresponding to the coherent intergrowth of the "1201" cuprate, S_2CC oxycarbonate, and (100) collapsed phase are evidenced.

INTRODUCTION

The recently isolated superconducting copper oxycarbonates belong to a fascinating class of materials, characterized by remarkable behavior since they usually exhibit a critical temperature T_c which is higher than those of the parent structures. They are generated by two classical structural mechanisms that are intergrowths of different structural units and shearings. These mechanisms are favored by the high flexibility of the layered cuprate frameworks (see Ref. (1) for a review), and result in a very rich microstructure. More than 20 superconducting oxycarbonates are now known which can be classified into three structural families.

The structure of the first family, drawn in Fig. 1a, simply results from the intergrowth of one 1201 member of layered cuprates, $A_{1-x}M_xSr_2CuO_{5-\delta}$, with one or several copper oxycarbonate slices, $Sr_2CuO_2CO_3$, termed S_2CC. The different members can be expressed through the general formulation $[S_2CC]_n[1201]$. The parameters of the tetragonal cell of the $[S_2CC]_1[1201]$ oxycarbonates are $a \approx a_p \approx 3.85$ Å (a_p is the parameter of the ideal cubic perovskite cell) and $c \approx c_{1201} + c_{S2CC} \approx 16.5$ Å. The first synthesized compound, $Tl_{0.5}Pb_{0.5}Sr_4Cu_2O_7CO_3$ (2), exhibits an intermediate rock salt-type layer $[Tl_{0.5}Pb_{0.5}O]$ which consists in randomly distributed thallium and lead cations. Other $[S_2CC]_1[1201]$ oxycarbonates have been isolated, with A = Tl or Hg and M = Bi, Cr, Mo, V, or Pb (3–7).

The structural characteristics of the second family have been discovered in $TlSr_{4-y}Ba_yCu_2O_7CO_3$ with $1 \leq y \leq 2$ (8–10). This oxycarbonate exhibits an orthorhombic supercell with $a \approx a_p$, $b \approx 8a_p$, $c \approx 17$ Å and A-type symmetry. The superstructure along **b** results from the periodic formation, in the $[S_2CC]_1[1201]$ structure, of (100) crystallographic shear planes (CSP), every four octahedra (Fig. 1b and c). These oxycarbonates have been therefore called "(100) collapsed oxycarbonates." Through the CSPs, the [TlO] ribbons are connected to the [CO] layers, according to the following sequence: four [TlO] rows alternate with four rows of carbonate groups along **b**. As a result, an alternative mode to describe the structure is to consider that the 1201-type framework remains unchanged but that the intermediate layers are ordered $[Tl_4C_4O_8]$ layers.

Varying the Ba/Sr ratio, a third family has been observed, which only differs from the second family by the orientation and the periodicity of the CSPs, which are (110) planes (Fig. 1d and 1e). They are called the "(110) collapsed oxycarbonates" (11–12).

In the (100), as well as in the (110), collapsed oxycarbonates, the periodicity of the CSPs can be expressed through **m** which represents the number of A cations or carbonate rows between two CSPs. Complex intergrowths of integer members have been observed, so that **m** is not necessarily an integer. Up to now, regular members for $3 \leq \mathbf{m} \leq 6$ have been characterized: (110) CSPs are observed for $4.5 \leq \mathbf{m} \leq 6$ whereas (100) CSPs are observed for $3 \leq \mathbf{m} < 4.5$.

Although almost nothing is understood about the structural transitions between the three families, it is most likely that geometrical factors, and especially the size of the cations in the $[(Ba, Sr)O]_\infty$ layers, play an important role in the stabilization of these different materials. This is the case of the superconducting oxycarbonates $Hg_{1-x}V_xSr_{4-y}Ba_yCu_2O_{7-\delta}CO_3$ (13), for which the three structural types have been isolated, depending on the y values. This sug-

[1] To whom correspondence should be addressed.

0022-4596/96 $18.00

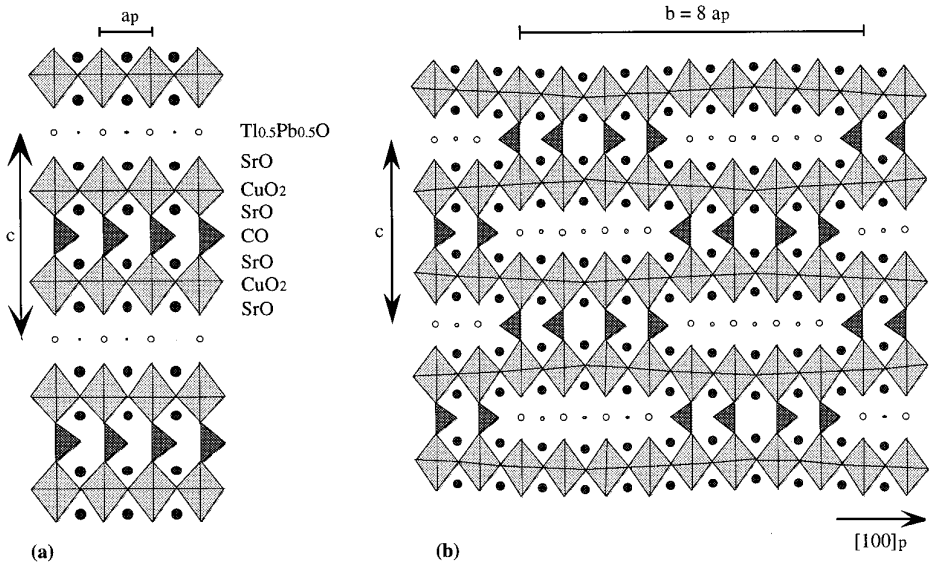

(100) collapsed

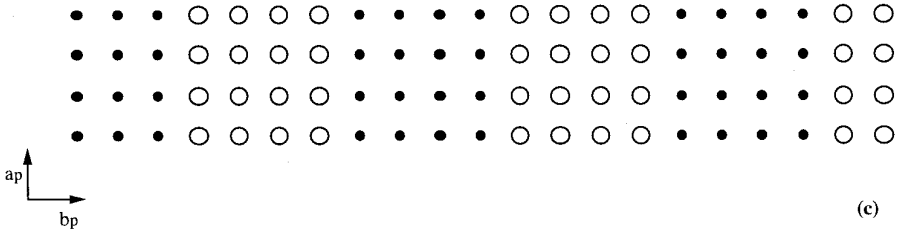

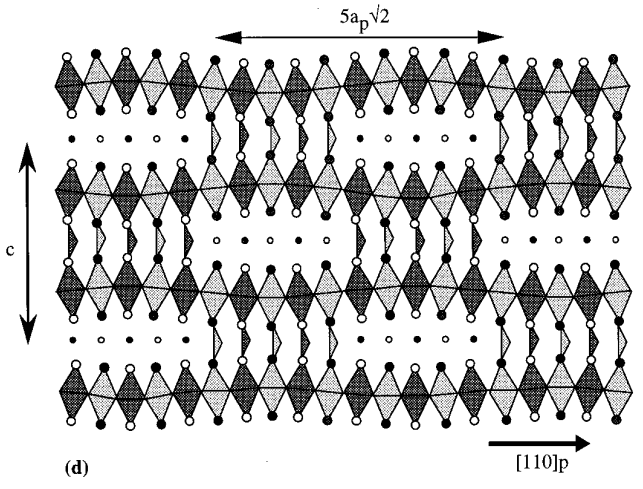

(110) collapsed

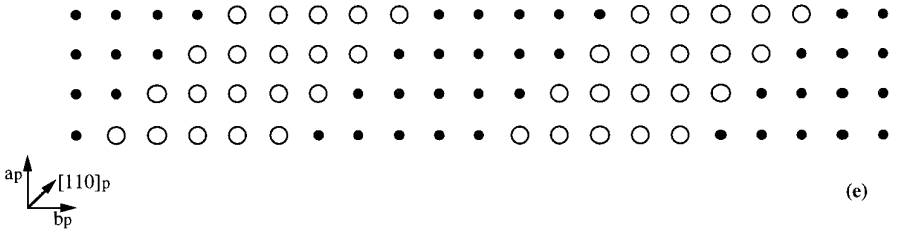

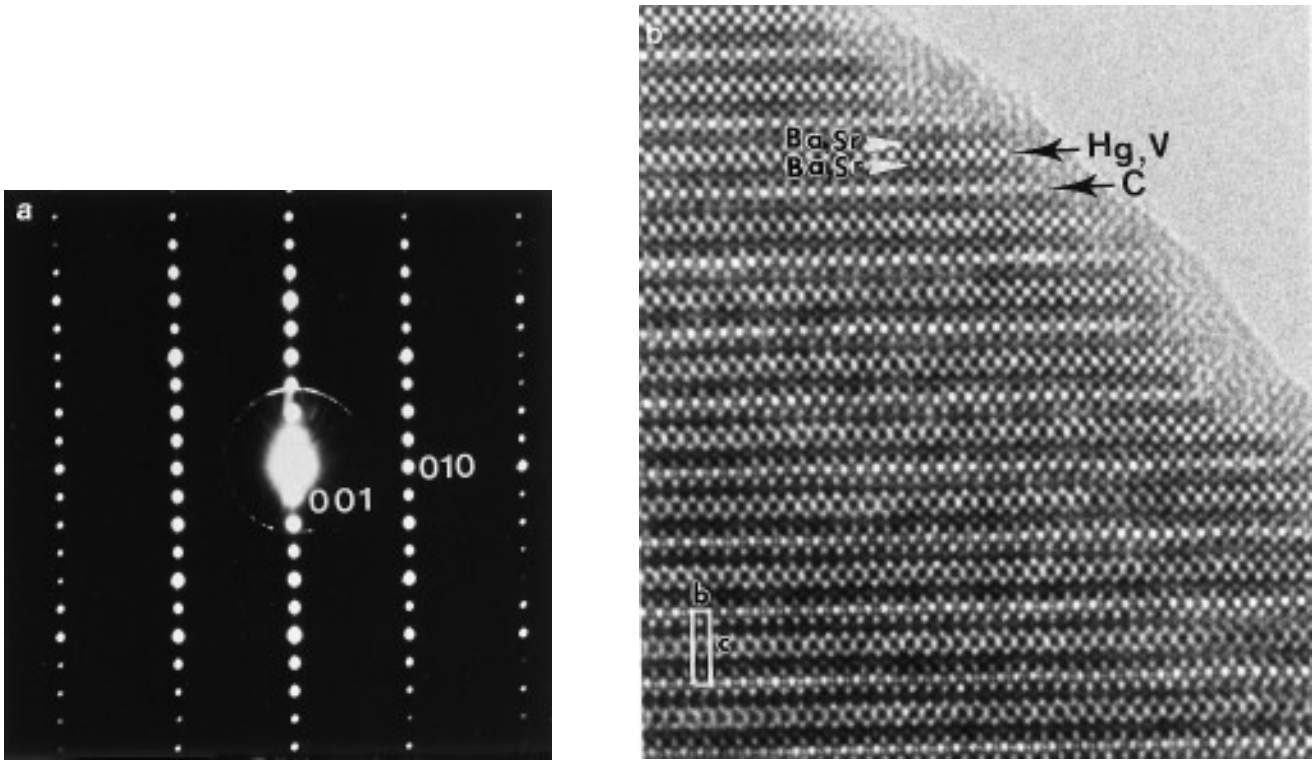

FIG. 2. $Hg_{0.6}V_{0.4}Sr_4Cu_2CO_3O_{7-\delta}$: (a) [100] ED pattern and (b) corresponding HREM image showing the regular layer sequence in the [S2CC] [1201] structure.

gests a very high flexibility of the structure of these phases with regard to the shearing phenomena and raises the issue of the shearing mechanism at the scale of the nanostructure. We report herein on the HREM study of these oxycarbonates that evidences for the first time nonplanar crystallographic shear boundaries (CSB) that originate from the combination of (100), (110), and even ($hk0$) crystallographic shear planes (CSP).

Previous Results on the Synthesis and Homogeneity Range of the Oxycarbonates $Hg_{1-x}V_xSr_{4-y}Ba_yCu_2O_{7-\delta}CO_3$

The mercury vanadium oxycarbonates $Hg_{1-x}V_xSr_{4-y}Ba_yCu_2O_{7-\delta}CO_3$ were prepared as previously reported (13), starting from the stoichiometric ratio of HgO, V_2O_5, CuO, BaO_2, Sr_2CuO_3, and $SrBaCuO_2CO_3$.

The electron diffraction (ED) study was performed with JEOL 200CX and 2010 electron microscopes and the high resolution electron microscopy (HREM) study was performed with a TOPCON 002B microscope, having a point resolution of 1.8 Å. The three microscopes are equipped with EDS analyzers. Image calculations were carried out with the Mac Tempas software.

The electron diffraction investigation showed that the three structural types of oxycarbonates are stabilized:

—For $0 \leq y < 1.8$, a $[S_2CC]_1[1201]$ structure is obtained. The subcell is tetragonal with $a = a_p$ and $c \approx 16.5$ Å and P-type symmetry.

—For $1.8 < y < 2.5$, a (110) collapsed structure is observed. The cell is orthorhombic with $a \approx a_p\sqrt{2}$, $b \approx m \cdot a_p\sqrt{2}$ if m is an integer and $2m \cdot a_p\sqrt{2}$ if m is half an integer, $c \approx 16.9$ Å, and exhibits A-type symmetry.

—For $2.5 < y \leq 2.65$, a (100) collapsed structure is observed. The cell is orthorhombic with $a \approx a_p$, $b \approx 2m \cdot a_p$, $c \approx 17$ Å, and A-type symmetry.

—For samples with $y > 2.65$, isolated (100) collapsed-type grains have been characterized by ED but the majority phases are the 1201 cuprate, $Hg_{1-x}V_xSr_{2-y}Ba_yCuO_{5-\delta}$ (14), and the copper oxycarbonate, $Sr_{2-y}Ba_yCuO_2CO_3$ (15).

The limits of the three structural types within the oxycar-

FIG. 1. The superconducting oxycarbonates $A_{1-x}M_xSr_{4-y}Ba_yCu_2CO_3O_7$. (a) Structure of the $[S_2CC]$ [1201] intergrowth projected along [100]. (b) Structure of the $m = 4$ member of the (100) collapsed phase family projected along [100]. The carbonate groups are drawn as dark triangles. (c) Schematical representation (only the positions of the cations are considered) of the intermediate mixed (001) layer built up from alternating infinite ribbons of C and Hg(V), parallel to [100]. The open circles represent the Hg and V atoms whereas the carbon atoms are small black circles. (d) Structure of the $m = 5$ member of the (110) collapsed phase family projected along $[1\bar{1}0]_p$ and (e) schematical representation of the (001) mixed layer. The C and Hg(V) ribbons are parallel to $[1\bar{1}0]$.

bonate homogeneity range are schematized as

$x = 0.4$ 0.35 0.3 0.28

I----------I----------I----I .

$y = 0$ 1.8 2.5 2.65

↑ ↑ ↑ ↑

S_2CC-1201 $(110)_{col}$ $(100)_{col}$

RESULTS

1. Nanostructures of the [S_2CC] [1201] Oxycarbonate

The HREM investigation of the $[S_2CC]_1[1201]$ oxycarbonate, $Hg_{1-x}V_xSr_{4-y}Ba_yCu_2O_{7-\delta}CO_3$, for $0 \leq y < 1.8$ and $0.35 < x \leq 0.4$, first evidences that the Hg/V distribution within the intermediate layer as well as the Ba/Sr distribution is randomly ensured. Second, it shows that the stacking of the two parent structures, 1201 and S_2CC, is very regular. These observations are illustrated by the [100] ED pattern and HREM image displayed in Fig. 2. The contrast interpretation was made using image calculations, carried out from the XRD refined parameters (13). The cation positions are imaged as dark dots (Fig. 2b), so that the mixed Hg/V layers appear as rows of very dark dots whereas the carbonate layers appear as rows of very small grey dots separated by very bright dots (these rows are two types indicated by black arrows in the image). These two types of layer are sandwiched between mixed [(Ba, Sr)O] layers, which also appear as rows of dark dots (white arrows). At the level of the mixed Hg/V and Ba/Sr layers, the high regularity of the contrast attests that no short range ordering takes place between Hg and V, on one hand, and/or Ba and Sr, on the other hand.

The superstructure. The reconstruction of the reciprocal space shows that, within the whole domain, i.e., $0 \leq y < 1.8$, weak extra reflections are observed in the ED patterns. This feature is illustrated in the three patterns displayed in Fig. 3 where the extra reflections are indicated by white

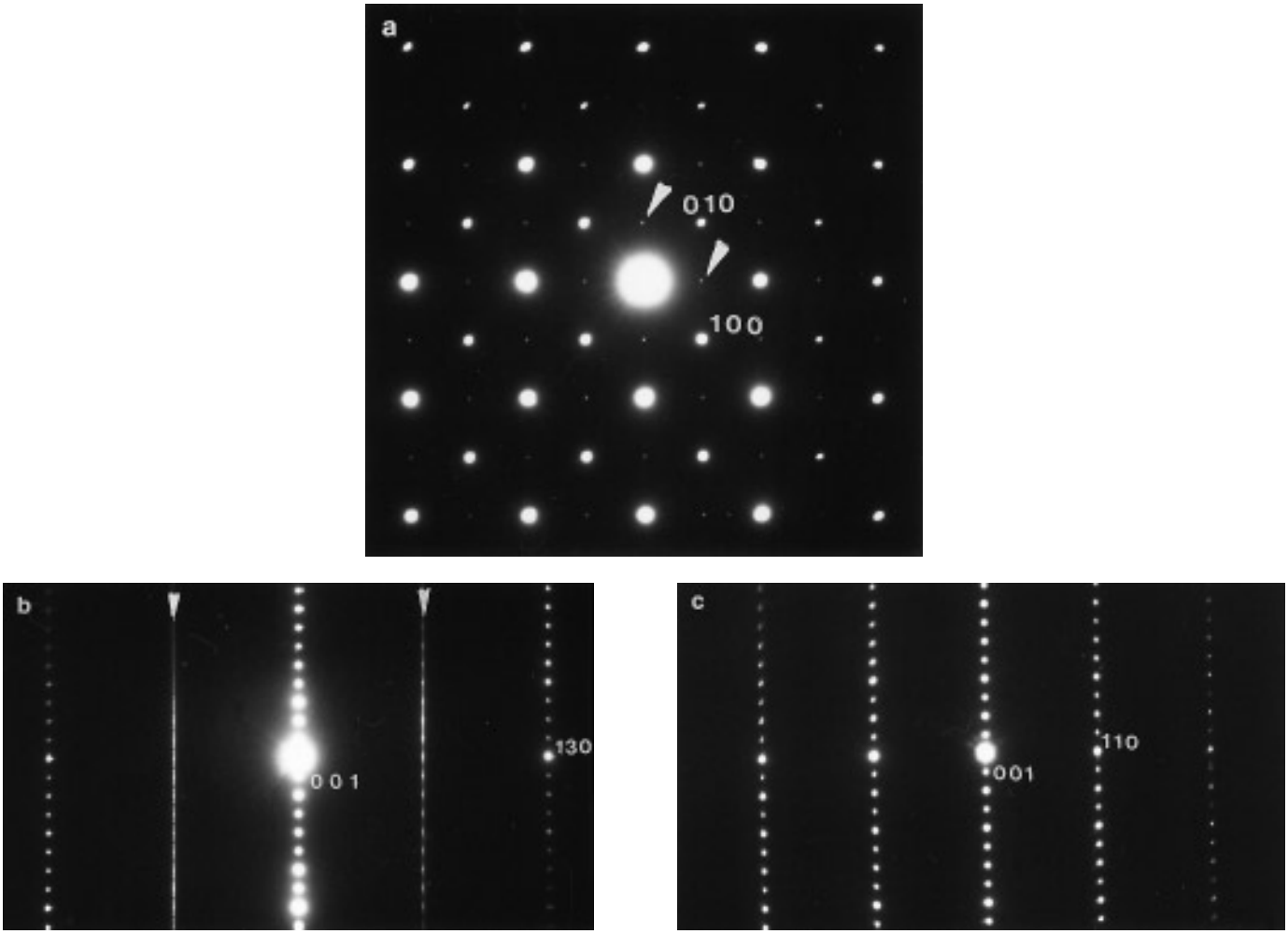

FIG. 3. (a) [001], (b) $[3\bar{1}0]$, and (c) $[1\bar{1}0]$ ED patterns showing the supercell parameters. The patterns are indexed in the tetragonal cell with $a \approx 3.8$ Å and $c_{S2CC-1201} \approx 16.5$ Å.

arrows. These patterns are indexed in the tetragonal subcell. In the [001] ED pattern (Fig. 3a) the extra reflections are at positions $\frac{1}{2}\ \frac{1}{2}\ 0$ (white arrows). In the $[3\bar{1}0]$ pattern (Fig. 3b), one observes the superposition of two different systems of extra spots: in the first, they are at positions $\frac{1}{2}\frac{1}{2}0$ and in the second at positions $\frac{1}{2}\,0\,0$. Such a superposition can be easily explained on the basis of two structural hypotheses: either the presence of 90° oriented domains or the coexistence of two superstructure variants. Note that the extra reflections are often streaked along c^*. In the $[\bar{1}10]$ pattern, no extra reflection is observed (Fig. 3c). Taking into consideration the conditions limiting the reflection in the whole reciprocal space, these extra reflections can be indexed according to two modes.

The first takes into consideration the coexistence of two different superstructures of the tetragonal subcell: one centered tetragonal supercell with $a_I \approx a\sqrt{2} \approx a_p\sqrt{2}$ and $c_I = 2c$ and one P-type tetragonal supercell with $a_{II} \approx a\sqrt{2} \approx a_p\sqrt{2}$ and $c_{II} = c$ (a and c being the parameters of the tetragonal $[[S_2CC]_1[1201]$ subcell). The two variants would be systematically present in every crystal.

The second mode is based on an orthorhombic supercell with $a_0 \approx b_0 \approx a\sqrt{2} \approx a_p\sqrt{2}$ and $c_0 = 2c$. The conditions limiting the reflection are $h_0k_0l_0$, $k_0 + l_0 = 2n$, and $0k_0l_0$, $k_0' = 2n$, involves $Abmm$ and $Abm2$ as possible space groups. Every crystal is twinned because the superstructure would systematically arise along the two equivalent [110] directions of the tetragonal subcell.

Since neither the I- nor the P-type tetragonal supercell has been observed separately and because the twinned orthorhombic supercell allows the use of a single indexation set, the second mode, i.e., the orthorhombic A-type supercell, will be considered. In the centered [001] pattern (Fig. 3a), the $0k_00$ reflections with $k_0 = 2n + 1$ appear as a result of the twinning phenomenon and double diffraction. The superstructure and the twinning phenomena are clearly observed along the oblique zone $[3\bar{1}0]$ of the tetragonal $[S_2CC]_1[1201]$ subcell. The corresponding images show that the structural phenomenon which is responsible for the superstructure takes place at the level of the carbonate layers. An example is shown in Fig. 4 where the carbonate layers are imaged as rows of bright dots, running in a direction perpendicular to **c**, while the other layers appear as continuous bright fringes. These bright dots are spaced 2.3 Å apart, which is in agreement with a doubling of the d_{130} in the tetragonal subcell and corresponds to the d_{120} of the orthorhombic supercell. The corresponding ED pattern (Fig. 3b) corresponds in fact to the superposition of the $[\bar{1}20]_0$ and $[2\bar{1}0]_0$ zones of the orthorhombic supercell. Along **c**, two adjacent bright dots are either aligned or in staggered position, due to the twinning micro phenomenon. These positions are indicated by black circles in the image (Fig. 4). It clearly appears that the stacking of the two variants is randomly distributed. These observations

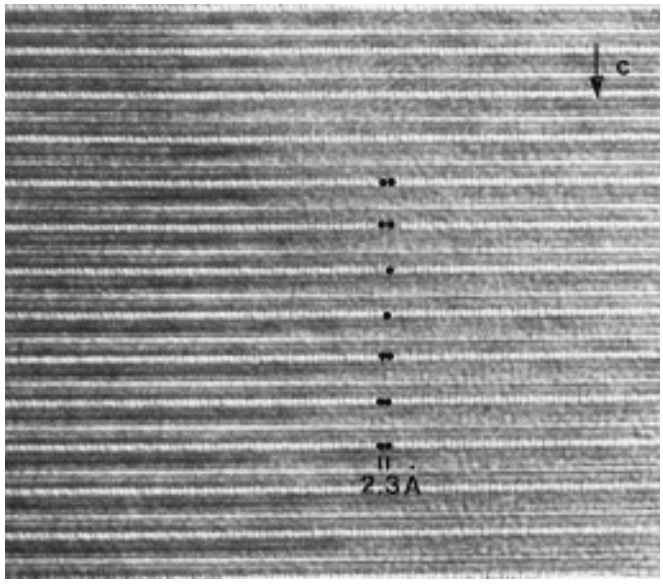

FIG. 4. $[3\bar{1}0]$ HREM image showing that the short-range ordering correlated with the extra reflections in the ED patterns arises at the level of the carbonate layers. The carbonate layers appear as rows of bright dots.

are similar to those made previously for $Sr_2CuO_2CO_3$ (16–19) that showed that beside the body-centered supercell "$2a_p \times 2_{a_p} \times 2c$" there exists a second structural variant based on a primitive lattice $a_p\sqrt{2} \times a_p\sqrt{2} \times c$. Thus, a similar ordering of the orientation of the CO_3 groups within the carbonate layers can be proposed for the intergrowth $[S_2CC]_1$ [1201] in agreement with the model proposed for the S_2CC structure (19).

Defects in the $[S_2CC]_1[1201]$ *oxycarbonates.* In a general way, few defects are observed in the mercury–vanadium $[S_2CC]_1[1201]$ oxycarbonates. The [100] image displayed in Fig. 5a, recorded for a $y = 0$ crystal, is interesting since all the types of defects which have been observed in these materials coexist within a single area. The carbonate layers are imaged as rows of bright dots. Linear defects are observed parallel to c; they are indicated by triangles subscripted **1**. Through these lines, the carbonate rows are shifted by $c/2$ so that the defects can be easily interpreted as resulting from (010) crystallographic shearing planes. The dark lines therefore correspond to the "tracks" of the CSP, viewed along [100]. Three structural points characterize these CSP in the $[S_2CC]_1[1201]$ matrix:

—They do not cross the whole crystal but are generally limited to a few tens of nanometers long.

—The extremity of the CSP defect is accommodated by the existence of a second type of defect that is the formation of two adjacent $[S_2CC]$ layers, i.e., the member $[S_2CC]_2[1201]$. It allows the compensation of the $c/2$ shifting. They are indicated by small white arrows and a schematic drawing is displayed in Fig. 5b. Sometimes, the CSP

is translated along **b** by a few octahedra so that the $[S_2CC]_2[1201]$ member is formed only over a few octahedra long. As an example, such a phenomenon is observed in the top of Fig. 5a, appearing as a short very bright layer segment.

Beside these linear defects, one observes broader boundaries, the thicknesses of which are variable, as shown for instance in the area indicated by a triangle subscripted **2** (Fig. 5a). Such defects, where the white contrast of the carbonate layers is disturbed and even no longer visible, are assumed to correspond to an orientation of the CSP which is no longer parallel to the electron beam, i.e., different from the [100] direction. Thus, in such areas, the CSPs are no longer (100) but (*hk*0) and the apparent width of the defect depends on the CSP orientation and on the crystal thickness. This contrast is easily explained by considering the orientation of the electron beam with respect to the shear plane (Fig. 5c and 5d). When the electron beam is parallel to [100], the (010) shear planes are observed as linear tracks and the contrast variation due to the shifting is clear owing to the fact that along [100], only carbon atoms are aligned at one side of the boundary and only mercury and vanadium atoms at the other side (Fig. 5c). In contrast, if one supposes that the shear plane is (110)-type, one observes a variation of the contrast over several rows due to the fact that the C and Hg(V) atoms are projected over the same positions at the boundary which therefore appears as broad (Fig. 5d). As a consequence, one observes the superposition of the contrasts and the local strains due to the connection of the Hg(V) to the C layers. In this example, the calculated crystal thickness for a (110) CSP would be close to 65 Å, which is consistent with the experimental contrast.

When y tends toward 1.8, the transition between the noncollapsed $[S_2CC]_1[1201]$ and (110) collapsed structure appears to be ensured by progressively increasing the number of crystallographic shear planes in the matrices. An example of a $[\bar{1}10]$ pattern is given in Fig. 6 where the reflections exhibit an elongated shape (parallel to [110]*).

2. *Transition from the Noncollapsed to the* (*110*) *Collapsed* [S_2CC] [*1201*] *Structure:* $Hg_{0.65}V_{0.35}Sr_{2.2}Ba_{1.8}Cu_2O_{7-\delta}CO_3$

For $y = 1.8$, the overall images show that the CSP are established within every crystal and throughout the whole matrix but the boundaries, through which the carbonate and mercury layers are connected, are complex. The CSP spacing is highly variable so that the **m** value ranges between 50 and 11 (Fig. 7a) and moreover, the boundaries are often no longer linear.

Within one mixed (010) layer, the arrangement of the carbon and mercury (or V) atoms is no longer perfect, straight, and regular as in the (110) collapsed oxycarbonates (ideal model in Fig. 1e) with connections parallel to $[1\bar{1}0]$ and periodically spaced of m octahedra. The boundaries are often curved and wander in the matrix, changing in direction and sometimes adopting a ''hairpin'' configuration. That means that ''mixed CSPs'' are waving in the matrix; they result from the more or less frequent changes of direction of the shearing mechanism. Schematical drawings of the boundaries are displayed in Figs. 7b (viewed along **c**) and 7c (viewed along $[1\bar{1}0]$). Such complex shearings have been previously observed in other oxides such as in the nonstoichiometric WO_{3-x} oxides; in this latter case, it results in the formation of groups of a variable number of edge-sharing octahedra (20).

Moreover, the observation of the crystal along $[1\bar{1}0]$ shows that these boundaries are also curved in the third direction: the width between the connections is variable from one (001) layer to the adjacent layers so that the boundaries are not necessarily parallel to the $(1\bar{1}0)$ planes. The enlarged image in Fig. 7a illustrates these two points.

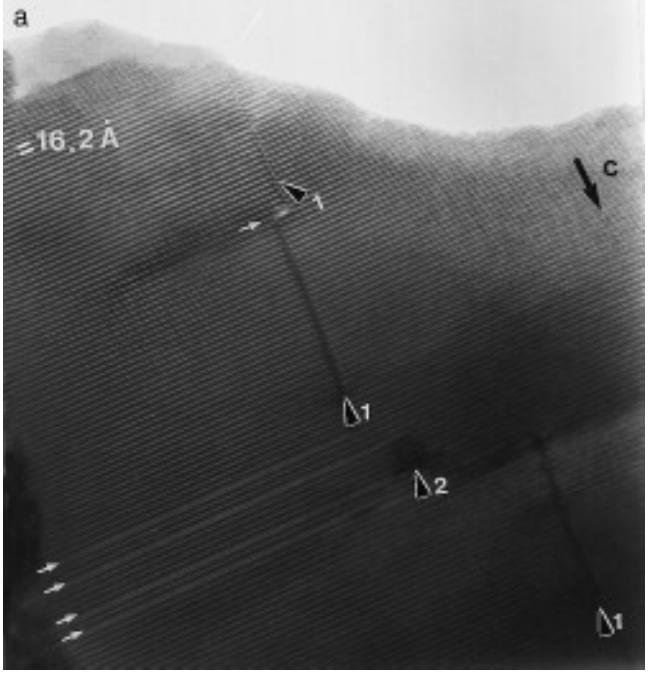

FIG. 5. (a) [100] HREM image showing the three types of defects observed in the $[S_2CC]$ [1201] matrix. The tracks of the CSP are indicated by triangles. The linear defects correspond to the tracks of the (010) CSP and are subscripted **1**. The broad boundaries (subscripted **2**) are assumed to correspond the existence of (1*k*0) CSP with $k \neq 0$. The $[S_2CC]_2$ [1201] members are indicated by white arrows. (b) Schematic drawing of an isolated (010) CSP defect. The CSP is parallel to the projection direction so that the track is represented as a dark line. The extremity of the defect is accommodated by the formation of a $[S_2CC]_2$ [1201] member. Schematic representations of a CSP defect crossing the (001) intermediate layer and of the resulting apparent thickness of the boundary viewed along [100]: (c) (010) CSP and (d) (110) CSP.

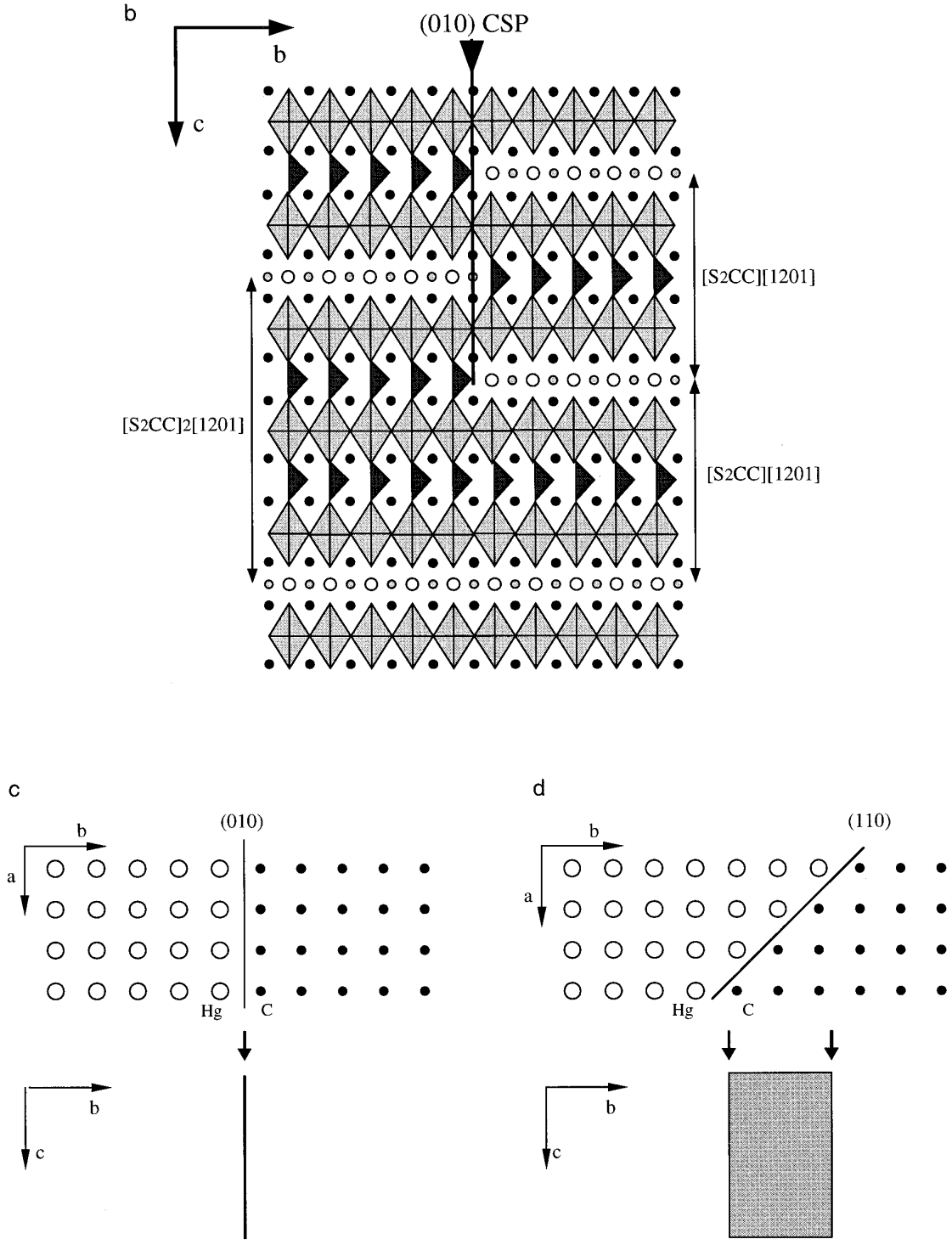

FIG. 5—*Continued*

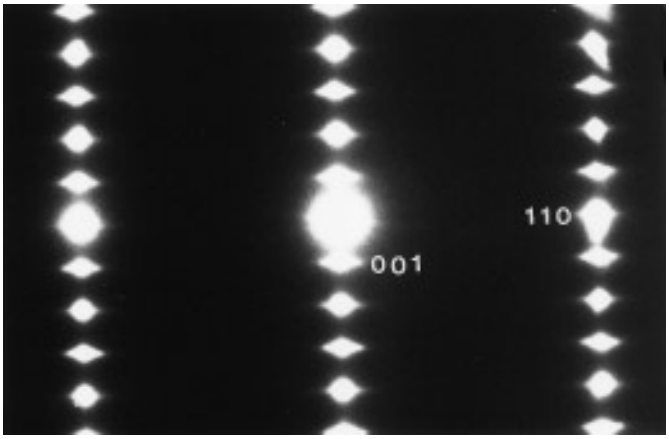

FIG. 6. [1$\bar{1}$0] ED pattern exhibiting elongated reflections along [110]* as a result of the existence of numerous CSP defects.

In these limit compositions, the connection periodicity progressively varies from one layer to the adjacent layers, as illustrated in Fig. 7c.

These results show the very high flexibility of the shearing planes that change continuously their orientation. As a consequence, the existence of curved crystallographic shear boundaries is evidenced for the first time which delimit volumes of variable shapes where the carbonates are shifted by $c/2$ with regard to the adjacent ones. Tilting about c^*, satellites are observed in all the [hk0] ED patterns, as a result of the 3D shape of the collapsed domains whereas in the ''pure'' (110) collapsed oxycarbonates they are only observed in the [110] patterns. Examples of [100] and [1$\bar{3}$0] patterns recorded for the same crystal are given in Figs. 8 and b, respectively.

3. *The* (110) *Collapsed Oxycarbonates*

For the crystals of actual composition in the range $1.8 < y < 2.5$, (110) CSP are systematically established throughout the crystals but the periodicity is, by far, not perfectly ensured. An example of [1$\bar{1}$0] HREM image, recorded for a $y = 1.9$ crystallite, and the corresponding ED pattern are shown in Figs. 9; the component of the modulation vector along [110]* is close to 0.083. If the average periodicity along [110] is close to 33 Å $= 12a_p\sqrt{2}/2$, i.e., the periodicity corresponding to the $m = 6$, the distribution of the carbonate groups (white dots in Fig. 9a) is not regular since one observes layers with 7 or 8 adjacent carbonate groups (instead of 6) whereas in another there are only 4 or 5. This average m value is the highest observed up to now.

When the barium content increases, **m** decreases down to an average value close to 4.5, similarly to what is observed in the other (110) collapsed oxycarbonates.

4. *Transition from the* (110) *Collapsed to the* (100) *Collapsed Structure*: $Hg_{0.7}V_{0.3}Sr_{1.5}Ba_{2.5}Cu_2CO_3O_{7-\delta}$

The systems of satellites observed for crystals corresponding to y close to 2.5, $Hg_{0.7}V_{0.3}Sr_{1.5}Ba_{2.5}Cu_2CO_3O_{7-\delta}$, are again very complex. Numerous crystals have been characterized, combining ED, EDS, BF imaging for different tilting angles, and HREM selecting [100], [1$\bar{1}$0], and [001] orientations. This investigation shows that the common feature is the existence of domains but there is no crystal archetype. Some examples would illustrate the main nanostructural features observed in the transition composition.

In areas where only the (110) collapsed structure is established, 90° oriented domains are systematically observed. The existence of these domains is clearly observed in the [001] ED patterns; an example is shown in Fig. 10. The satellites (indicated by small white arrows) are lying along [110*] and [$\bar{1}$10]*. The corresponding images show that the domain size is variable, ranging from ten to a few hundred nanometers. Note that in these crystals, numerous microcracks are observed.

The reconstruction of the reciprocal space, carried out by tilting about c^*, shows that, in most of the crystals, satellites are observed whether the crystal orientation may be but with variable intensities. The [$\bar{1}$10] and [$\bar{1}$20] ED patterns recorded for one crystal are given in Figs. 11a and 11b, respectively. The fact that satellites are observed in every [hk0] pattern indicates that, again, the cation ordering is no longer established along one single direction (**b** or [110]) so that the infinite parallel ribbons of carbonate groups and the Hg(V) atoms, running along [100] (Fig. 1c) or [1 $\bar{1}$ 0] (Fig. 1d), do not exist anymore. The different directions of the cation ordering were evidenced in the [001] images, recorded in the thin part of the crystal (in thicker parts, the overlapping of the domains leads to a disturbed contrast). The shape and the size of these domains can be observed by comparing all the images recorded for the different tilting angles in the course of the rotation around c^*. It appears that the domain sizes range, as for the [110] twinning domains, from a few tens to a few hundreds of nanometers. The atomic arrangement in such domains, and the connection through the two types of boundaries, is schematically drawn in Fig. 11c. An example of adjacent large domains is given in Fig. 12a with two ordering directions: the modulation along [110] is observed in the right part of the image whereas it is observed along [010] in the left part. The coexistence of very small domains is shown in Fig. 12b. Domains oriented 90° where the (100) collapsed structure is established over a few nanometers are observed; the orientation of the domains is indicated in the image through the **b** axes (small white arrows). The boundaries between the domains are not straight and the domain shape is not geometrical. However, in this image, it clearly appears that in some areas, the modulation direc-

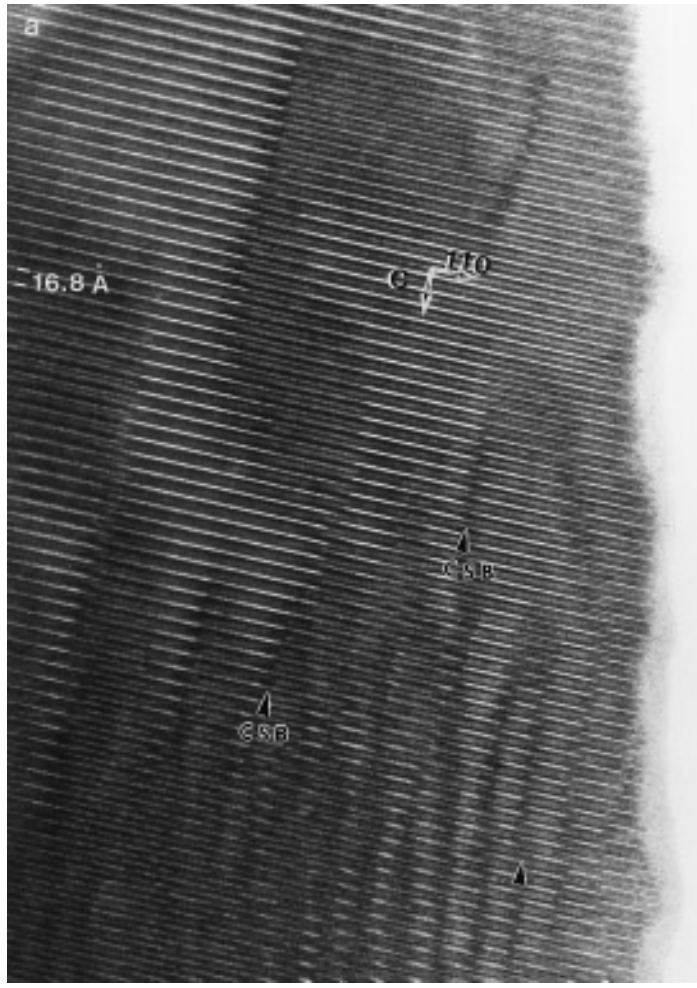

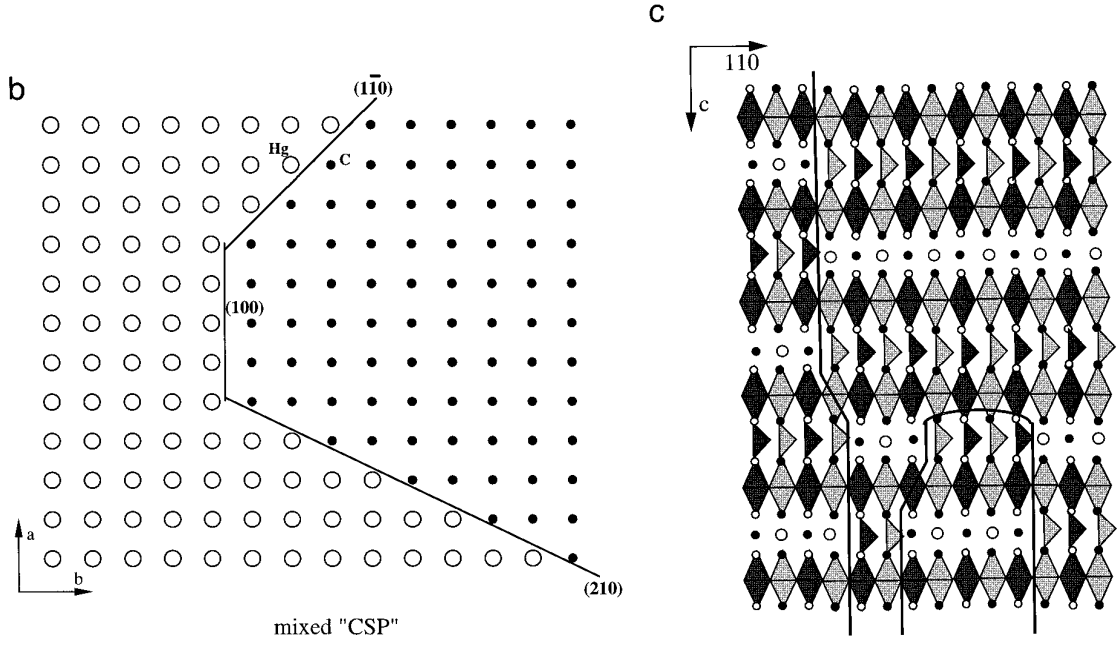

FIG. 7. $Hg_{0.65}V_{0.35}Sr_{2.2}Ba_{1.8}Cu_2CO_3O_{7-\delta}$: formation of complex crystallographic shear boundaries (CSB). (a) [110] HREM image where some of the CSB are indicated by triangles. (b) Schematic drawing of the CSB resulting from the change in direction and spacing of the shearing planes at the level of the (001) mixed intermediate layer. (c) Schematic drawing viewed along [1$\bar{1}$0]. The boundaries are drawn as dark lines.

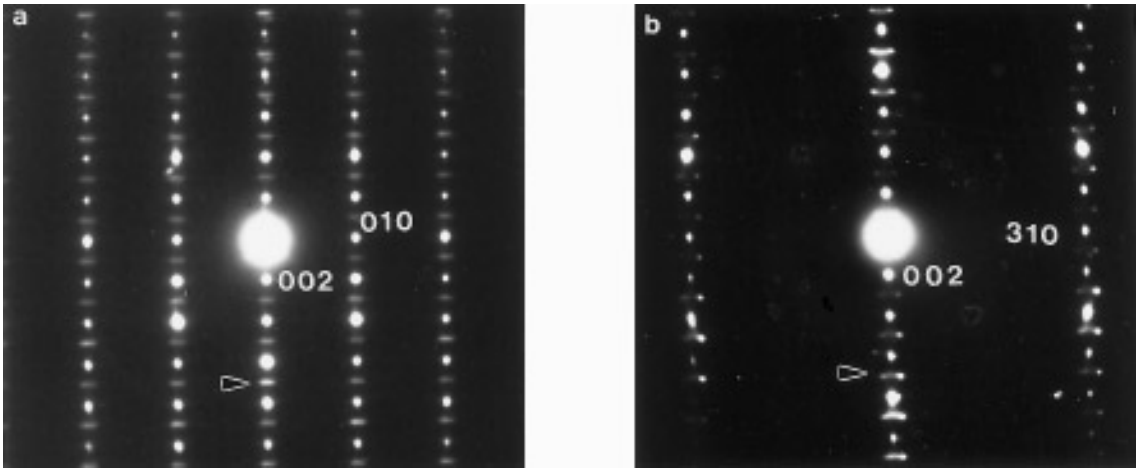

FIG. 8. $Hg_{0.65}V_{0.35}Sr_{2.2}Ba_{1.8}Cu_2CO_3O_{7-\delta}$: (a) [100] and (b) [$\bar{1}$30] ED patterns recorded by tilting about c^*.

tion is about 20° misoriented with regard to the adjacent ones, i.e., it arises along [310]. The atomic distribution of a mixed layer where the boundary is parallel to [310] is schematically represented in Fig. 11d. The corresponding ED pattern (Fig. 12c) exhibits weak satellites lying mainly along the a^* and b^* directions of the tetragonal subcell. Moreover, it can be seen that the intense reflections of the subcell are split in several spots, suggesting that the different domains exhibit common a^* and b^* directions but are characterized by small parameter variations. This can be understood by refering to the evolution of a and b parameters vs y; in the (100) collapsed domain ($y > 2.5$), a rapid increase of these parameters with y is indeed observed (13).

The average periodicity of the majority of these ''mixed collapsed'' crystals is close to 32 Å as well along b as [110], i.e., corresponding to an average m value of 6 along [110] in the (110) collapsed small domains and 4 along **b** in the (100) collapsed small domains.

5. *The (100) Collapsed Oxycarbonates*

For higher barium content ($y > 2.5$), (100) crystallographic shear planes are established. For $y = 2.55$, m values close to 5 are usually observed. An example of a [100] ED pattern and the corresponding HREM image are given in Figs. 13a and 13b. For the latter image, the copper layers are imaged as rows of bright dots; the strong undulation of the copper planes resulting from the interatomic distance variations between Hg(V)–O and C–O can be easily observed. An $m = 5$ value is observed for the first time in the (100) collapsed phases, since the higher value of regular

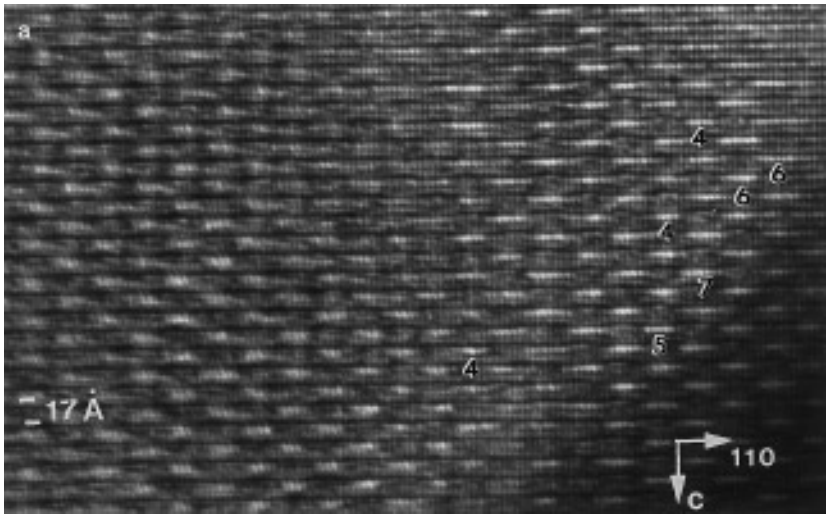

FIG. 9. $Hg_{0.65}V_{0.35}Sr_{2.1}Ba_{1.9}Cu_2CO_3O_{7-\delta}$: (a) the HREM image and (b) the corresponding ED pattern.

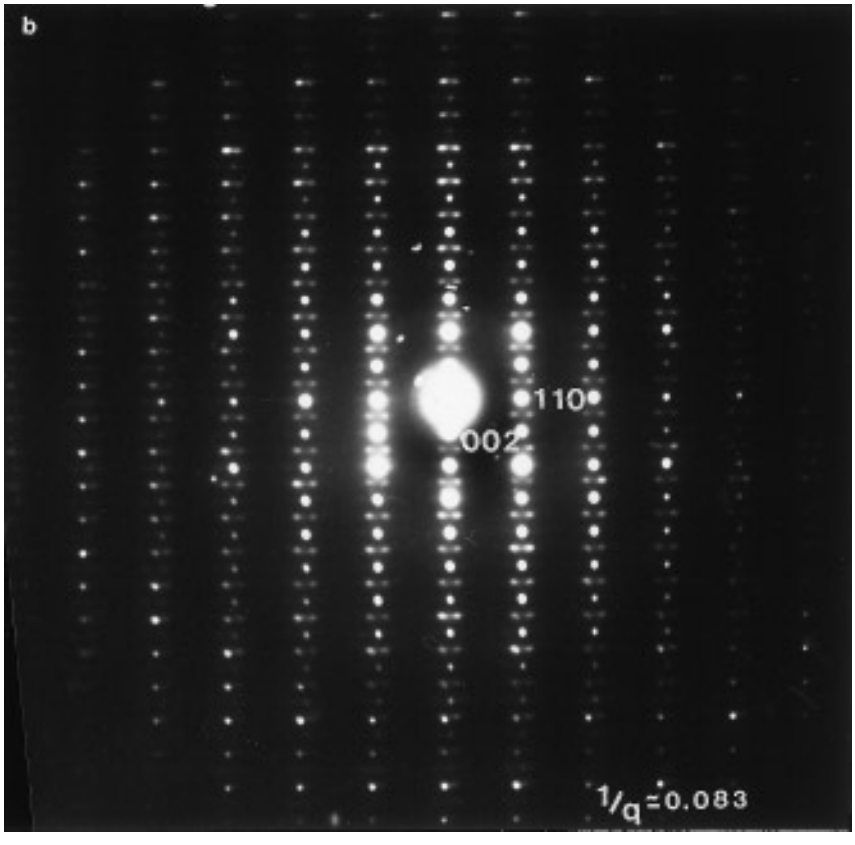

FIG. 9—*Continued*

(or almost regular) members was observed to be $m = 4$. Locally, defective larger members are formed (arrowed in Fig. 13b).

As mentioned for the (110) collapsed oxycarbonates, one observes that the average periodicity of the modulation, $b = 2m \cdot a_p$, tends to decrease when the barium content increases but grains of highly regular m values are rarely observed. For the limit composition, $y = 2.65$, numerous grains are observed where (100) ribbons with width m ranging from 2 to 4 are randomly distributed. One example is shown in the [100] image in Fig. 14, where the number of adjacent carbonate groups is indicated.

6. *Samples with $y > 2.65$*

As previously mentioned, for $y > 2.65$, X-ray and electron diffraction show that oxycarbonates are still formed but the majority phases are barium rich $Sr_{2-y}Ba_yCuO_2CO_3$ and $Hg_{1-x}V_xSr_{2-y}Ba_yCuO_{5-\delta}$ phases. The HREM investigation shows that the different phases are formed and coexist in domains within the same grain. An example is shown in Fig. 15 where the carbonate groups are imaged as bright dots. In the right part of the image, wide carbonate $Sr_{2-y}Ba_yCuO_2CO_3$ ribbons are observed and a few (100)

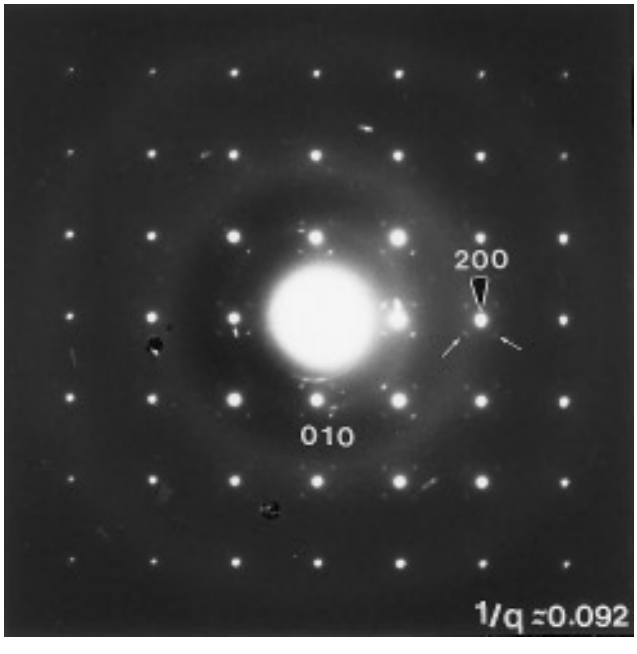

FIG. 10. [001] ED pattern of a twinned $Hg_{0.7}V_{0.3}Sr_{1.5}Ba_{2.5}Cu_2CO_3O_{7-\delta}$ crystal.

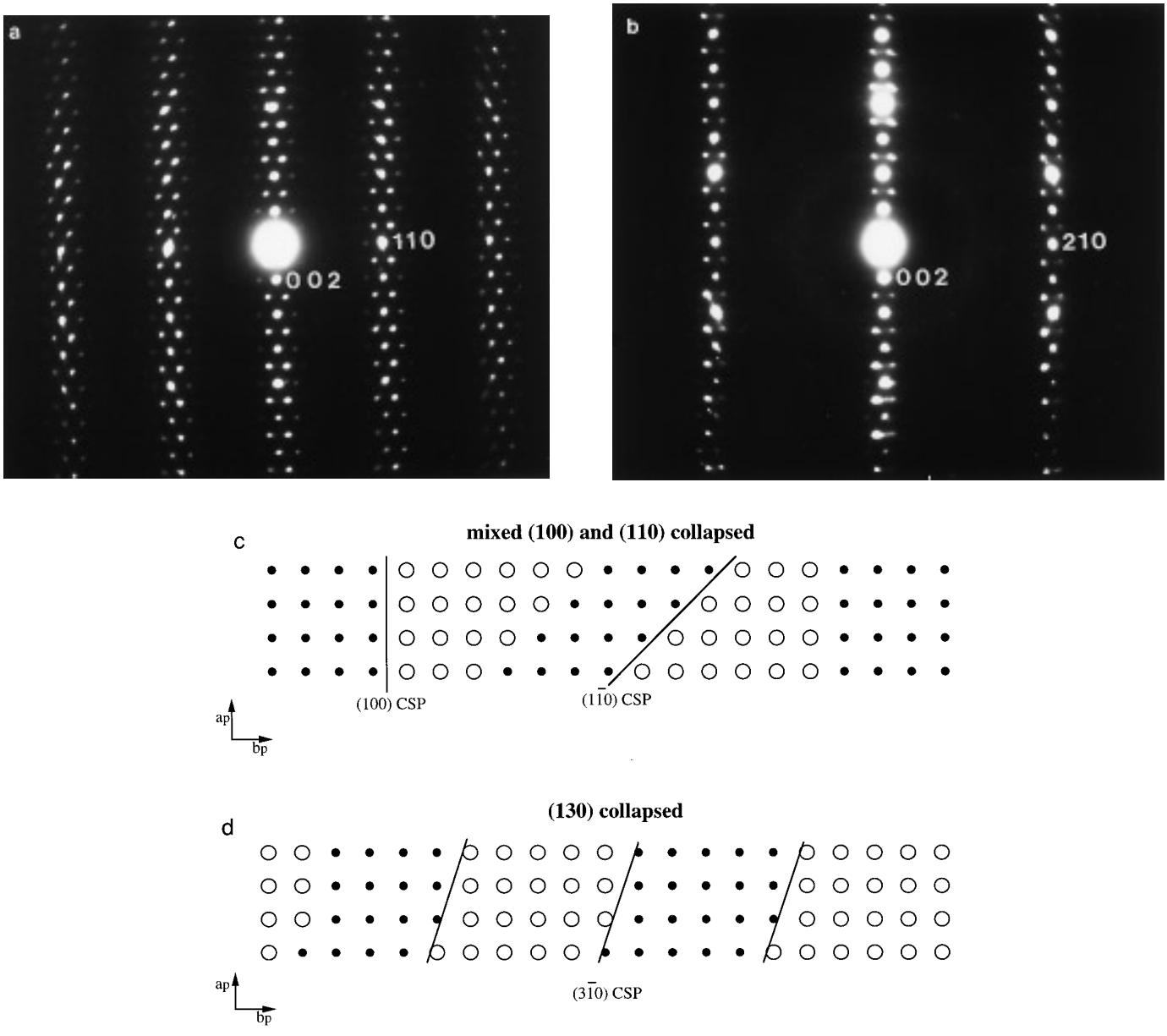

FIG. 11. $Hg_{0.7}V_{0.3}Sr_{1.5}Ba_{2.5}Cu_2CO_3O_{7-\delta}$: (a) [$\bar{1}$10] and (b) [$\bar{1}$20] ED patterns. Idealized drawing of intermediate (001) mixed layers where (c) (010) and (1$\bar{1}$0) CSP coexist and (d) where (13$\bar{0}$) CSP arise.

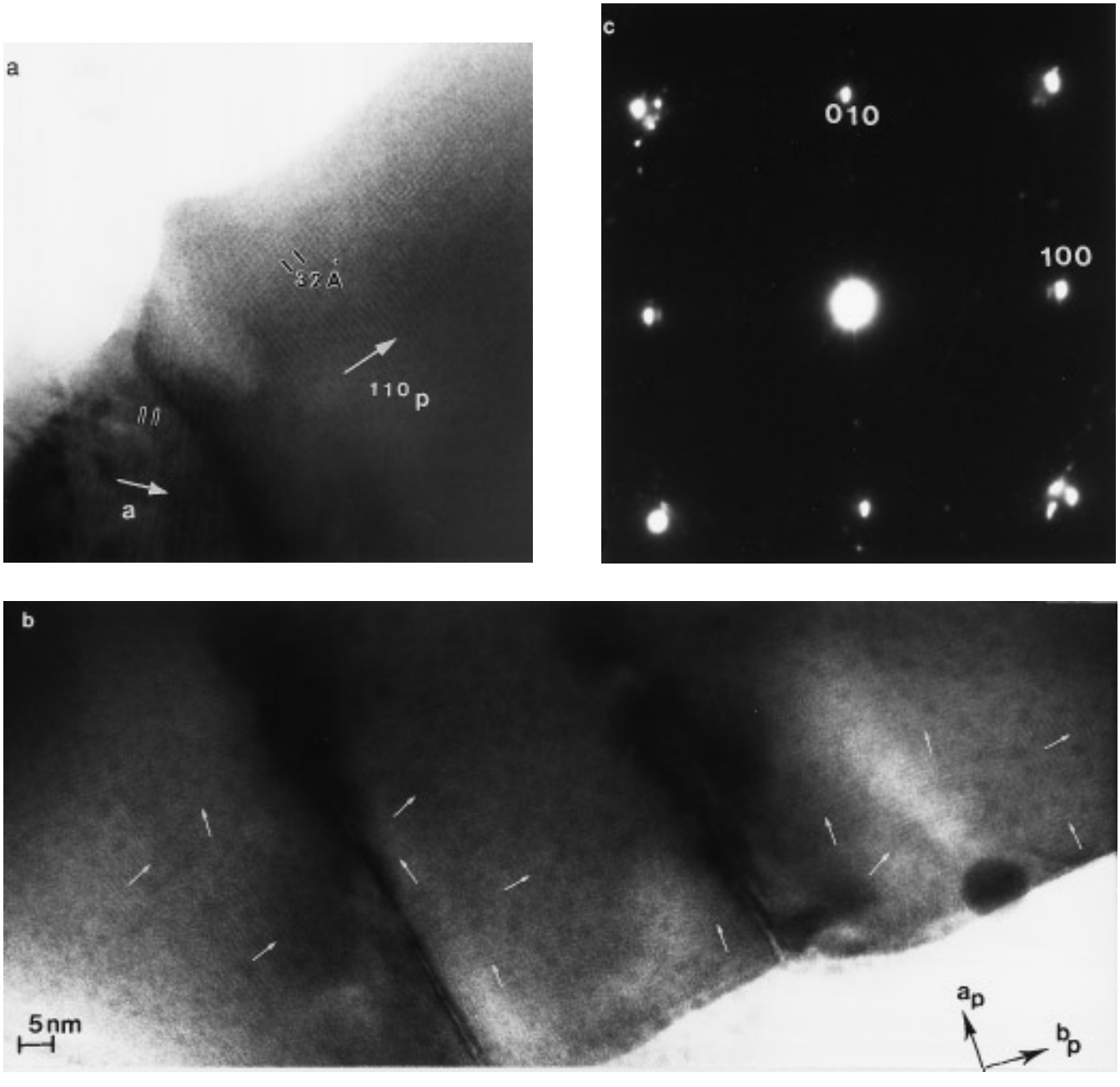

FIG. 12. $Hg_{0.7}V_{0.3}Sr_{1.5}Ba_{2.5}Cu_2CO_3O_{7-\delta}$. [001] HREM images illustrating the different types of domains. (a) Existence of large (100) and (110) collapsed domains. (b) Small ($1k0$) collapsed domains. The direction of the modulation is indicated by small white arrows in some of them. (c) The corresponding ED pattern.

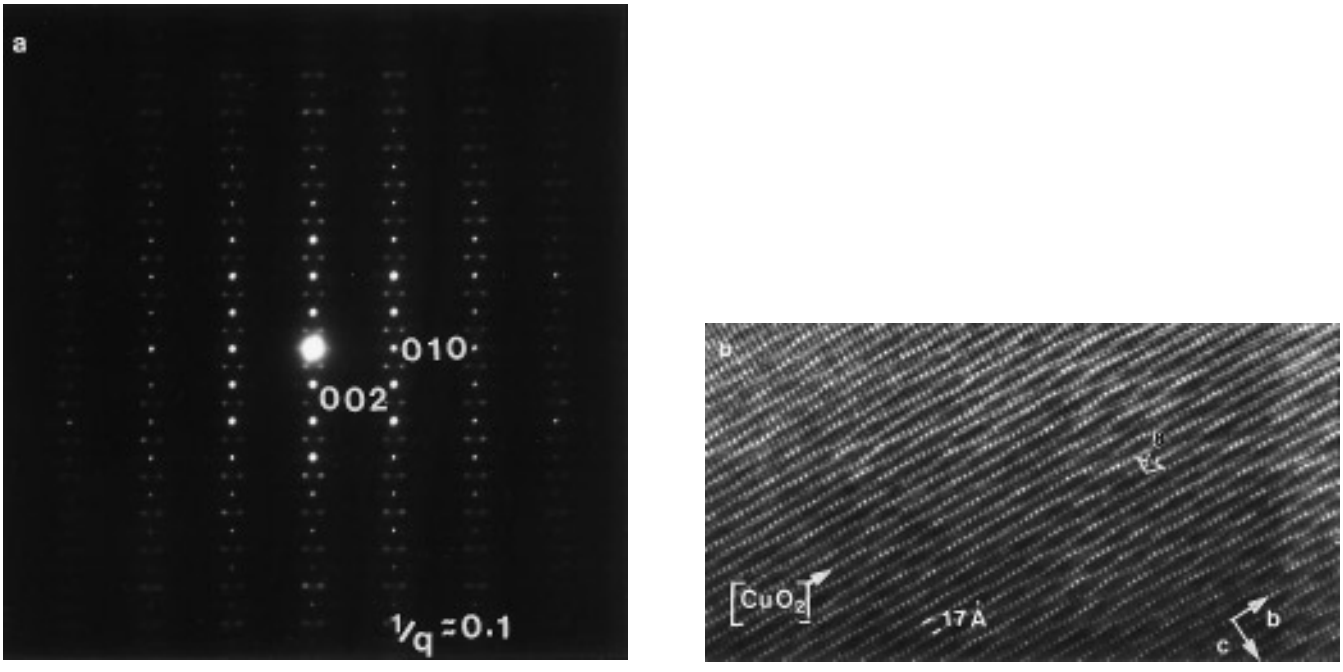

FIG. 13. The (100) collapsed oxycarbonate $Hg_{0.7}V_{0.3}Sr_{1.45}B_{2.55}Cu_2CO_3O_{7-\delta}$: (a) [100] ED pattern and (b) the corresponding HREM image. The copper layers $[CuO_2]$ are imaged as rows of bright dots. The *m* value of this (100) collapsed phase is close to 5.

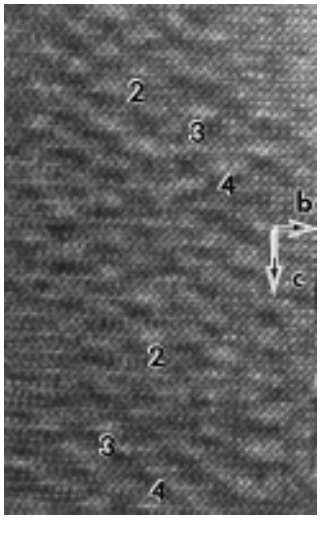

FIG. 14. $Hg_{0.72}V_{0.28}Sr_{1.35}Ba_{2.65}Cu_2CO_3O_{7-\delta}$. [100] image where different *m* members are randomly distributed. The carbonate groups appear as white dots.

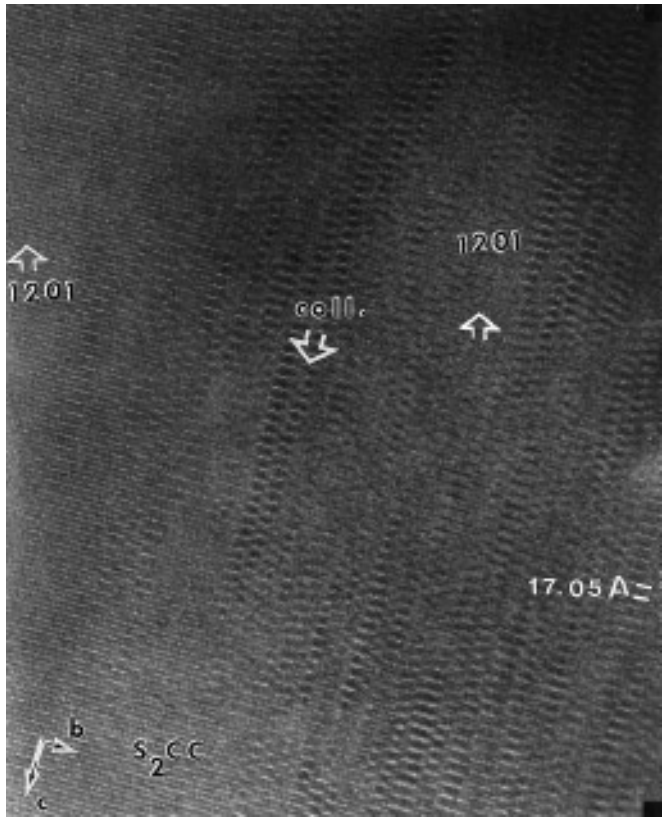

FIG. 15. [100] HREM image of a phasoïd observed for $y > 2.65$ where "1201," S_2CC, and (100) collapsed oxycarbonate coexist.

collapsed segments are in the middle, whereas the 1201 phase is established in the left part. Such crystals where 1201, $Sr_{2-y}Ba_yCuO_2CO_3$, and collapsed oxycarbonate coexist have been previously reported in $Hg_{1-x}Pb_xSr_{4-y}Ba_yCu_2O_{7-\delta}CO_3$ (11), describing the so-generated complex system of satellites.

DISCUSSION

This study demonstrates the extraordinary flexibility of the $[S_2CC]_1[1201]$ matrix with respect to the shearing mechanisms that this structure can accommodate. The possibility of coexistence of (100) and (110) CSP as defects in the same crystal is shown for the first time in superconducting oxycarbonates, whereas new kinds of CSP are evidenced, such as the (120) and (130) planes, that are stabilized in the form of small domains. Such complex behavior of the shearing phenomena can be compared to that observed in the shear structures of tungsten suboxides W_nO_{3n-2} (21) and of phosphate tungsten bronzes (22).

These observations show the very strong influence of the cation composition ratio, especially the Ba/Sr ratio, upon the shearing phenomena that appear in the matrix. As summarized in Fig. 16, one observes that starting from a pure intergrowth in the absence of barium ($y = 0$, Fig. 16a), the introduction of significant amount of barium ($0 < y < 1.8$) favors the formation of (100) and (110) CSP defects that coexist in the same matrix (Fig. 16b), leading to curved CSB for $y = 1.8$ (Fig. 16c), whereas the pure (110) collapsed is obtained for high barium contents

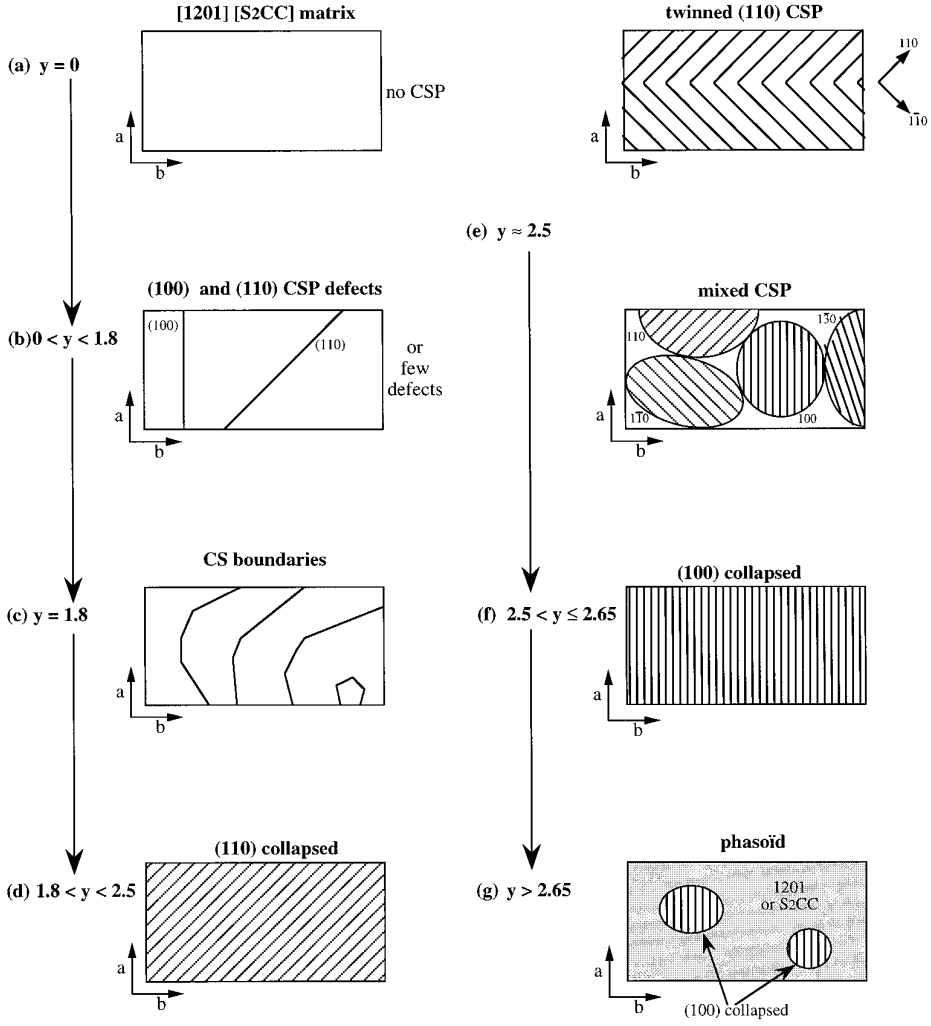

FIG. 16. Schematic representation of the evolution of the nanostructures in the course of the $[S_2CC]$ [1201] ⇔ (110) collapsed ⇔ (100) collapsed transitions. The shearing events are only drawn in the form of straight or curved and isolated or periodic lines. These lines represent the tracks of the crystallographic shear planes in the (001) intermediate mixed layer. The y values are indicated.

$1.8 < y < 2.5$ (Fig. 16d). Increasing the barium content further leads to the formation of twinning (110) CSP structures and to mixed (100) and (110) CSP, for y close to 2.5 (Fig. 16e), and then to the (100) collapsed structure for $2.50 < y \leq 2.65$ (Fig. 16f). Finally, for the highest barium content ($y > 2.65$), one obtains a coherent intergrowth of phasoïds, ''1201,'' S_2CC, and (110) collapsed and [S_2CC][1201] (Fig. 16g).

Another way to understand the influence of barium content upon the nanostructure of these materials is to consider that whatever y, ranging from 0 to 2.65, the structure can be considered a ''1201'' structure which consists of the intergrowth of mixed carbonate and mercury (vanadium) layers with pure octahedral copper layers as previously described for $TlSr_2Ba_2Cu_2O_7CO_3$ (8). In the absence of barium ($y = 0$) pure carbonate layers alternate with pure $[Hg_{1-x}V_xO_{1-\delta}]_\infty$ layers, whereas the introduction of barium tends to destabilize the pure carbonate layers at the benefit of mixed ''carbonate Hg(V)'' layers. This is supported by the fact that $Sr_2CuO_2CO_3$ is easily synthesized in contrast to $Ba_2CuO_2CO_3$. For a certain amount of barium ($1.8 < y < 2.50$) a long range ordering of the Hg(V) and CO_3 groups along [110] is favored leading to the (110) collapsed structure, whereas still increasing the barium content ($2.5 < y \leq 2.65$) favors a long range ordering along [100] leading to the (100) collapsed structure. Finally, for too high barium contents ($y > 2.65$), the long range ordering is destroyed. This leads progressively to $(Hg_{1-x}V_xO_{1-\delta})$ domains concentrated in barium rich regions forming locally the ''1201''-type structure $Hg_{1-x}V_xSr_{2-y}Ba_yCuO_{5-\delta}$, whereas carbonate groups are predominant in strontium regions forming $Sr_{2-y}Ba_yCuO_2CO_3$-type structure; the higher stability of $Hg_{1-x}V_xBa_2CuO_{5-\delta}$ compared to $Hg_{1-x}V_xSr_2CuO_{5-\delta}$ (which has not been synthesized to date) strongly supports this viewpoint.

The relative stability of the two (100) and (110) collapsed structures may be connected to the cation, and especially barium, distribution. A complete structure determination by neutron diffraction will be necessary to answer this issue, to bring also into consideration the possible influence of oxygen nonstoichiometry. In any case, all these phenomena do not involve the rupture of the copper–oxygen layers so that superconductivity is not dramatically influenced by their appearance.

REFERENCES

1. M. Hervieu, G. Van Tendeloo, C. Michel, D. Pelloquin and B. Raveau, *Microsc. Microanal. Microstruct.*, in press.
2. M. Huvé, C. Michel, A. Maignan, M. Hervieu, C. Martin, and B. Raveau, *Physica C* **205,** 219 (1993).
3. A. Maignan, M. Huvé, C. Michel, M. Hervieu, C. Martin, and B. Raveau, *Physica C* **208,** 149 (1993).
4. D. Pelloquin, M. Hervieu, C. Michel, A. Maignan, and B. Raveau, *Physica C* **227,** 215 (1994).
5. C. Martin, M. Hervieu, M. Huvé, C. Michel, A. Maignan, G. Van Tendeloo, and B. Raveau, *Physica C* **222,** 19 (1994).
6. D. Pelloquin, M. Hervieu, S. Malo, C. Michel, A. Maignan, and B. Raveau, *Physica C* **246,** 1 (1995).
7. A. Maignan, D. Pelloquin, S. Malo, C. Michel, M. Hervieu, and B. Raveau, *Physica C* **249,** 220 (1995).
8. F. Goutenoire, M. Hervieu, A. Maignan, C. Michel, C. Martin, and B. Raveau, *Physica C* **210,** 359 (1993).
9. Y. Matsui, M. Ogawa, M. Uehara, H. Nakata, and J. Akimitsu, *Physica C* **217,** 287 (1993).
10. M. Kikuchi, E. Oshima, N. Ohnishi, Y. Muraoka, S. Nakajima, E. Aoyagi, M. Ogawa, J. Akimitsu, T. Oku, K. Hiraga, and Y. Syono, *Physica C* **219,** 200 (1994).
11. M. Huvé, G. Van Tendeloo, M. Hervieu, A. Maignan, and B. Raveau, *Physica C* **231,** 15 (1994).
12. M. Uehara, S. Sahoda, H. Nakata, J. Akimitsu, and Y. Matsui, *Physica C* **222,** 27 (1994).
13. S. Malo, D. Pelloquin, A. Maignan, C. Michel, and B. Raveau, submitted for publication.
14. K. Knizek, S. Malo, D. Pelloquin, M. Hervieu, C. Michel, and B. Raveau, to be published.
15. A. R. Armstrong, H. S. Obhi, and P. P. Edwards, *J. Solid State Chem.* **106,** 120 (1993).
16. D. V. Fomichev, A. L. Kharlanov, E. V. Antipov, and L. M. Kovba, *Superconductivity* **3,** 126 (1990).
17. Y. Miyazaki, H. Yamane, T. Kajitani, T. Oku, K. Hiraga, Y. Morii, K. Fuchizaki, S. Funahashi, and T. Hirai, *Physica C* **191,** 434 (1992).
18. O. Milat, G. Van Tendeloo, S. Amelinckx, T. G. N. Babu, and C. Greavest, *J. Solid State Chem.* **109,** 5 (1994).
19. H. Nakata, J. Akimitsu, S. Katano, T. Minami, N. Ogita, and M. Udagawa, *Physica C* **255,** 157 (1995).
20. S. Iijima, *J. Solid State Chem.* **14,** 52 (1975).
21. W. Sahle and M. Sundberg, *Chem. Scripta* **16,** 163 (1980).
22. M. Hervieu, B. Domengès, and B. Raveau, *J. Solid State Chem.* **58,** 233 (1985).